

The Dynamics of Mesoscale Winds in the Upper Troposphere and Lower Stratosphere

JÖRN CALLIES

Department of Earth, Atmospheric, and Planetary Sciences, Massachusetts Institute of Technology, Cambridge, Massachusetts

OLIVER BÜHLER

Courant Institute of Mathematical Sciences, New York University, New York, New York

RAFFAELE FERRARI

Department of Earth, Atmospheric, and Planetary Sciences, Massachusetts Institute of Technology, Cambridge, Massachusetts

(Manuscript received 11 April 2016, in final form 27 July 2016)

ABSTRACT

Spectral analysis is applied to infer the dynamics of mesoscale winds from aircraft observations in the upper troposphere and lower stratosphere. Two datasets are analyzed: one collected aboard commercial aircraft and one collected using a dedicated research aircraft. A recently developed wave–vortex decomposition is used to test the observations' consistency with linear inertia–gravity wave dynamics. The decomposition method is shown to be robust in the vicinity of the tropopause if flight tracks vary sufficiently in altitude. For the lower stratosphere, the decompositions of both datasets confirm a recent result that mesoscale winds are consistent with the polarization and dispersion relations of inertia–gravity waves. For the upper troposphere, however, the two datasets disagree: only the research aircraft data indicate consistency with linear wave dynamics at mesoscales. The source of the inconsistency is a difference in mesoscale variance of the measured along-track wind component. To further test the observed flow's consistency with linear wave dynamics, the ratio between tropospheric and stratospheric mesoscale energy levels is compared to a simple model of upward-propagating waves that are partially reflected at the tropopause. For both datasets, the observed energy ratio is roughly consistent with the simple wave model, but wave frequencies diagnosed from the data draw into question the applicability of the monochromatic theory at wavelengths smaller than 10 km.

1. Introduction

Meteorologists have debated what physical processes shape the atmospheric energy spectrum in the mesoscale range since [Nastrom and Gage \(1985\)](#) observed a conspicuous flattening of the spectrum at these scales. These authors analyzed wind and temperature observations collected aboard commercial aircraft during the Global Atmospheric Sampling Program (GASP) and found spectra that roll off roughly like k^{-3} at synoptic scales and like $k^{-5/3}$ at mesoscales, where k is the along-track wavenumber. The steep roll off at synoptic scales, wavelengths larger

than about 500 km, is readily explained as resulting from a downscale potential enstrophy cascade of geostrophic turbulence ([Charney 1971](#)). There is less agreement on what dynamics cause the gentler roll off at smaller scales, in the mesoscale range.

Many explanations of the mesoscale spectrum rely on turbulent dynamics. An early proposal was that the mesoscale spectrum arises from an energy cascade from small convective plumes to large-scale geostrophic motions (e.g., [Gage 1979](#); [Lilly 1983](#); [Vallis et al. 1997](#)). A more recent explanation suggests that the mesoscale spectrum arises from frontogenetic dynamics at the tropopause, which modify the characteristics of geostrophic turbulence ([Tulloch and Smith 2006](#)). A third explanation contends that the flow at mesoscales can escape the rotational constraint and that energy is thus transferred to small scales in strongly nonlinear stratified turbulence (e.g.,

Corresponding author address: Jörn Callies, Massachusetts Institute of Technology, 77 Massachusetts Ave., Bldg. 54-1615, Cambridge, MA 02139.
E-mail: joernc@mit.edu

Lindborg 2006). In all these cases, Kolmogorov-type dimensional analysis predicts a $k^{-5/3}$ energy spectrum.

A power-law spectrum does not necessarily imply strongly nonlinear cascade dynamics, however, and a very different explanation was advanced early on: Dewan (1979) suggested that the mesoscale energy spectrum arises from a superposition of quasi-linear inertia-gravity waves. This proposition is supported by observations in the frequency and vertical wavenumber domains as well as by the analogy with the ocean, where inertia-gravity waves have long been thought to dominate at scales smaller than those dominated by geostrophic motions (e.g., VanZandt 1982). What determines the spectral shape in this scenario is largely unclear, but second-order nonlinear wave-wave interactions are known to result in power-law behavior and slopes around $-5/3$ (e.g., McComas and Müller 1981; Polzin and Lvov 2011). The hallmark of this explanation of the mesoscale energy spectrum is thus that the dynamics are to leading order linear, rather than that they imply a particular spectral slope.

To make progress and test theoretical predictions beyond the spectral slope, we recently developed a decomposition method applicable to one-dimensional aircraft observations (Bühler et al. 2014). Under the assumption of horizontal isotropy, the method first decomposes the horizontal kinetic energy spectrum into rotational and divergent components. Applied to the commercial aircraft data collected as part of the Measurement of Ozone and Water Vapor by Airbus In-Service Aircraft (MOZAIC) project, this Helmholtz decomposition shows that the mesoscale flow has a significant divergent component, ruling out theories relying solely on quasigeostrophic dynamics (Callies et al. 2014). This reduces the question of what dynamics govern the dominant mesoscale flows to whether they obey quasi-linear dynamics (inertia-gravity waves) or are strongly nonlinear (stratified turbulence).

To address this question, the method developed in Bühler et al. (2014) has a second step that attempts a wave-vortex decomposition based on the assumption that the flow is a superposition of geostrophic flow and linear inertia-gravity waves. The method provides a prediction of the total hydrostatic wave energy (horizontal kinetic plus potential) based on the observations of the horizontal velocities only. A comparison of this predicted total wave energy with the observed total energy is then a check on the consistency of the flow with the polarization and dispersion relations of inertia-gravity waves. Conversely, if the flow is strongly nonlinear—not satisfying polarization and dispersion relations—one would expect the predicted energy to differ from the observed energy. In Callies et al. (2014), we applied this procedure to the MOZAIC data and found that the

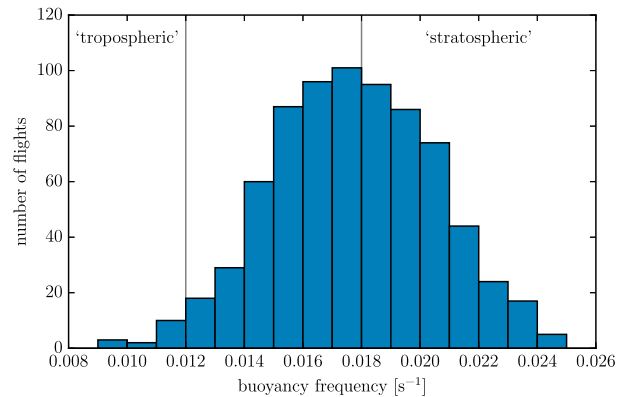


FIG. 1. Histogram of flight-average buoyancy frequency for MOZAIC flights with no selection for altitude as in Callies et al. (2014). The vertical lines indicate the thresholds for buoyancy frequency used in this paper for the classification of flight segments into tropospheric and stratospheric.

observations in the mesoscale range are consistent with inertia-gravity waves.

Lindborg (2015) also applied the Helmholtz decomposition—reformulated for structure functions—to the MOZAIC data. He separated the data into tropospheric and stratospheric, using a threshold ozone concentration of 200 ppbv. For structure functions in both the troposphere and the stratosphere, he found a significantly larger rotational than divergent component at mesoscale separations, with a more pronounced dominance of the rotational component in the troposphere. A dominance of rotational kinetic energy would be inconsistent with inertia-gravity waves, which cannot have more rotational than divergent kinetic energy, but no such simple statement holds for the corresponding structure functions (cf. the appendix).

In Callies et al. (2014), we did not separate the data into altitude ranges but instead used all available flight tracks of sufficient length and data quality (cf. the appendix). The spectra presented there include both tropospheric and stratospheric data but are dominated by the more numerous tracks in the lower stratosphere (Fig. 1). Unlike the structure functions shown by Lindborg (2015), the spectra presented in Callies et al. (2014) exhibit a rough equipartition between the rotational and divergent components of horizontal kinetic energy over a wide mesoscale range, with a slight dominance of the divergent component at wavenumbers around $k = 2\pi/100$ km. As confirmed by the wave-vortex decomposition, this is consistent with inertia-gravity waves dominating the mesoscale range.

The apparent discrepancy between the energy spectra of Callies et al. (2014) and the structure functions of Lindborg (2015) can be fully explained by the relationship

between structure functions and spectra, as illustrated in detail in the [appendix](#). Briefly, structure functions contain the same information as spectra, but they are not optimal to study energy distributions scale by scale. Structure functions are not necessarily spectrally local (e.g., [Babiano et al. 1985](#)): the structure function at a certain separation r is not always indicative of the energy spectrum at wavenumber $k = r^{-1}$. If the energy spectrum is steep enough, the structure function at separation r instead corresponds to energy at wavenumbers much smaller than $k = r^{-1}$. This well-known property of structure functions demands caution when interpreting structure functions obtained from aircraft observations. We show in the [appendix](#) that, while the spectra of [Callies et al. \(2014\)](#) exhibit approximate equipartition between rotational and divergent kinetic energies at mesoscale wavenumbers k , the structure functions corresponding to these spectra have a clearly dominant rotational component at mesoscale separations r . The dominance of the rotational component in the structure functions at mesoscale separations r is due to leakage of synoptic-scale rotational energy and thus not reflective of mesoscale dynamics. This resolves the apparent inconsistency between [Callies et al. \(2014\)](#) and [Lindborg \(2015\)](#).

Questions remain, however, regarding the differences in mesoscale dynamics between the lower stratosphere and upper troposphere. This will be explored with spectral analysis in this paper. Before applying the wave–vortex decomposition method to tropospheric and stratospheric data, we investigate whether the method still works in the vicinity of a sharp tropopause, where the assumption of vertical homogeneity does not strictly apply. Using a simple model of upward-propagating linear inertia–gravity waves partially reflected at the tropopause, we investigate what the method predicts for a vertically inhomogeneous wave field in the upper troposphere. We show that a simple and robust wave–vortex decomposition result can still be obtained from our method, provided that the altitudes of the flight tracks are randomly distributed in the vicinity of the tropopause, which induces a certain random-phase averaging of the vertical wave structure.

We then split the MOZAIC data into tropospheric and stratospheric and confirm that there is relatively more rotational mesoscale energy in the troposphere than in the stratosphere, qualitatively consistent with [Lindborg \(2015\)](#). This result, however, is challenged by a dataset obtained as part of the 2008 Stratosphere–Troposphere Analyses of Regional Transport (START08) campaign (cf. [Pan et al. 2010](#); [Zhang et al. 2015](#)). In the upper troposphere, these data show a clear dominance of divergent flow in the mesoscale range, in

contrast to the MOZAIC data. The inconsistency between the two datasets casts doubt onto the result obtained from the MOZAIC data and calls for an inquiry into the accuracy of the wind measurements and the data processing. We discuss the respective advantages of the two datasets and suggest that, while we have high confidence in the START08 data, more analysis of other datasets is needed to fully understand the mesoscale dynamics in the upper troposphere.

In addition to the wave–vortex decomposition, the consistency of the observed mesoscale flow with linear inertia–gravity waves can be checked by considering the ratio between mesoscale energies above and below the tropopause. This ratio can be predicted with the simple model of partially reflected, upward-propagating linear inertia–gravity waves mentioned above. We show that the observed ratios are roughly within the range of ratios predicted by linear wave theory.

The paper is organized as follows. [Section 2](#) summarizes and extends the decomposition method developed in [Bühler et al. \(2014\)](#) and introduces the notation. [Section 3](#) investigates the theoretical situation near a sharp tropopause and computes the detailed wave structure and wave energies above and below the tropopause. The following sections discuss the decomposition and energy ratios of the MOZAIC data ([section 4](#)) and the START08 data ([section 5](#)). Inconsistencies between the datasets and their respective merits are discussed in [section 6](#). [Section 7](#) summarizes and concludes. The [appendix](#) discusses the relation between structure functions and spectra and the differences in interpretation.

2. Decomposition method

In [Bühler et al. \(2014\)](#), we introduced a method consisting of two parts. First, a Helmholtz decomposition separates the one-dimensional spectrum of horizontal kinetic energy into a rotational part and a divergent part. Second, a wave–vortex decomposition separates the one-dimensional spectrum of total energy (kinetic plus potential) into a geostrophic part and a wave part. If all assumptions (discussed below) are satisfied, this method yields the same energy partition as [Bartello's \(1995\)](#) projection of three-dimensional flow fields onto geostrophic and wave modes. The new method, however, only requires one-dimensional flow data that are readily available from observations.

a. Helmholtz decomposition

The Helmholtz decomposition operates on the observable density-weighted one-dimensional spectra of the horizontal velocity components along the track u and across the track v :

$$S^u(k) = \langle \rho_0 |\hat{u}(k)|^2 \rangle, \quad S^v(k) = \langle \rho_0 |\hat{v}(k)|^2 \rangle, \quad (1)$$

where the caret denotes a Fourier transform, ρ_0 is the mean density along the flight segment, and the angle brackets are an average over an ensemble of segments.¹ Both altitude z and time t are considered fixed, and the rationale for the density weighting is discussed in section 3 below.

To derive the decomposition in spectral space, we start with a conventional Helmholtz decomposition in physical space:

$$u = -\frac{\partial \psi}{\partial y} + \frac{\partial \phi}{\partial x}, \quad v = \frac{\partial \psi}{\partial x} + \frac{\partial \phi}{\partial y}, \quad (2)$$

where ψ denotes the streamfunction, ϕ denotes the velocity potential, and x and y denote the along- and across-track coordinates, respectively. In Fourier space, these equations yield the two-dimensional spectra of u and v in terms of the two-dimensional spectra of ψ and ϕ :

$$S^u(k, l) = l^2 S^\psi(k, l) - 2klC^{\psi\phi}(k, l) + k^2 S^\phi(k, l) \quad (3)$$

and

$$S^v(k, l) = k^2 S^\psi(k, l) + 2klC^{\psi\phi}(k, l) + l^2 S^\phi(k, l), \quad (4)$$

where l is the across-track wavenumber and $C^{\psi\phi}(k, l)$ is the cospectrum

$$C^{\psi\phi}(k, l) = \text{Re} \langle \rho_0 \hat{\psi}^*(k, l) \hat{\phi}(k, l) \rangle, \quad (5)$$

the asterisk denoting a complex conjugate. If the flow is statistically isotropic—that is, if $S^\psi(k, l)$, $S^\phi(k, l)$, and $C^{\psi\phi}(k, l)$ depend on $k_n = (k^2 + l^2)^{1/2}$ only—integration over the across-track wavenumber l yields

$$S^u(k) = D^\psi(k) - k \frac{d}{dk} D^\phi(k) \quad \text{and} \quad (6)$$

$$S^v(k) = -k \frac{d}{dk} D^\psi(k) + D^\phi(k), \quad (7)$$

where we defined the spectral functions

$$D^\psi(k) = \int_{-\infty}^{\infty} l^2 S^\psi(k, l) dl \quad \text{and} \quad (8)$$

$$D^\phi(k) = \int_{-\infty}^{\infty} l^2 S^\phi(k, l) dl, \quad (9)$$

which represent the rotational component of $S^u(k)$ and the divergent component of $S^v(k)$, respectively. Contrary to what we stated in Bühler et al. (2014), the requirement that streamfunction and potential be uncorrelated is not needed as long as the flow statistics are isotropic. If the cospectrum $C^{\psi\phi}(k, l)$ depends on k_n only, the integrand $klC^{\psi\phi}(k, l)$ is odd in l , and thus the integral over l of this cross term vanishes.

Using decay conditions as $k \rightarrow \infty$, the ODEs in (6) and (7) can be solved for $D^\psi(k)$ and $D^\phi(k)$ explicitly, which achieves the Helmholtz decomposition of the horizontal kinetic energy spectrum

$$K(k) = \frac{1}{2} [S^u(k) + S^v(k)] \quad (10)$$

into a rotational part and a divergent part:

$$K^\psi(k) = \frac{1}{2} \left(1 - k \frac{d}{dk} \right) D^\psi(k) \quad \text{and} \quad (11)$$

$$K^\phi(k) = \frac{1}{2} \left(1 + k \frac{d}{dk} \right) D^\phi(k). \quad (12)$$

Lindborg (2015) pointed out that (6) and (7) can be combined to

$$2 \frac{d}{dk} [kK^\psi(k)] = k \frac{d}{dk} S^v(k) + S^u(k) \quad \text{and} \quad (13)$$

$$2 \frac{d}{dk} [kK^\phi(k)] = k \frac{d}{dk} S^u(k) + S^v(k), \quad (14)$$

which can be integrated to give (using integration by parts and the assumption that all spectra vanish as $k \rightarrow \infty$)

$$2K^\psi(k) = S^v(k) + \frac{1}{k} \int_k^\infty [S^v(\kappa) - S^u(\kappa)] d\kappa \quad \text{and} \quad (15)$$

$$2K^\phi(k) = S^u(k) - \frac{1}{k} \int_k^\infty [S^v(\kappa) - S^u(\kappa)] d\kappa. \quad (16)$$

These explicit formulas are equivalent to (11) and (12), with $D^\psi(k)$ and $D^\phi(k)$ given as the solutions to (6) and (7), both analytically and in practice when applied to discrete observational data (cf. Bierdel et al. 2016).

b. Wave–vortex decomposition

If the flow is a superposition of geostrophic flow and linear inertia–gravity waves, then the total energy spectrum can be written

$$E(k) = \frac{1}{2} [S^u(k) + S^v(k) + S^w(k) + S^b(k)] \\ = E_g(k) + E_w(k), \quad (17)$$

¹ We adopt the convention that the number of arguments of spectra and Fourier transforms determines the number of dimensions of these quantities. We denote one- and two-dimensional spectra by the same symbol S^i , for example, distinguishing them by writing $S^i(k)$ for the one-dimensional and $S^i(k, l)$ for the two-dimensional spectrum.

where the geostrophic part is decorated with a subscript g and the wave part with a subscript w ;

$$S^w(k) = \langle \rho_0 |\hat{w}(k)|^2 \rangle \quad \text{and} \quad S^b(k) = \left\langle \frac{\rho_0}{N^2} |\hat{b}(k)|^2 \right\rangle \quad (18)$$

are the vertical velocity spectrum and the potential energy spectrum, with b denoting buoyancy and N the buoyancy frequency (averaged over the flight segment).

Plane or slowly varying linear waves obey the energy partition statement

$$2K_w^\psi(k) + S_w^b(k) = 2K_w^\phi(k) + S_w^w(k), \quad (19)$$

such that the total wave energy is given by

$$E_w(k) = 2K_w^\phi(k) + S_w^w(k). \quad (20)$$

For nearly hydrostatic waves, the $S_w^w(k)$ contributions to $E_w(k)$ and to the right-hand side of (20) are negligible. In that case, we are left with

$$E_w(k) = 2K_w^\phi(k), \quad (21)$$

which is the relation used in Böhler et al. (2014) and Callies et al. (2014). If vertical velocity measurements are also available, as is the case for the START08 data analyzed below, the full nonhydrostatic decomposition in (20) can be used.

Given the Helmholtz decomposition, $K^\phi(k)$ is known from the observed $S^w(k)$ and $S^v(k)$. It can be attributed to the wave component, because the geostrophic flow is horizontally nondivergent. Similarly, the vertical velocity spectrum $S^w(k)$, if available, can also be attributed to the wave component, because geostrophic flow is purely horizontal (the Coriolis parameter f is considered constant). If the flow is indeed a superposition of geostrophic flow and inertia–gravity waves, (17) can be used to diagnose the total energy of the geostrophic flow as the residual of the observed total energy and the diagnosed wave energy,

$$E_g(k) = E(k) - E_w(k), \quad (22)$$

and the wave–vortex decomposition of the total energy spectrum is thus complete.

Below, this wave–vortex decomposition will be used to test whether the dominant flow is consistent with linear wave dynamics in the mesoscale range, where the horizontal kinetic energy has a significant divergent component. If the mesoscale flow is supposed to be dominated by linear waves, the wave energy spectrum diagnosed with (20) or (21) constitutes a prediction of the total energy spectrum based on velocity

measurements only. If the *observed* total energy spectrum $E(k)$ then matches this prediction, the observed spectra are consistent with the dispersion and polarization relations of inertia–gravity waves. If the observed $E(k)$ does not match the prediction, the flow either has geostrophic and wave components that are comparable in magnitude, or the assumption that the flow is a superposition of geostrophic flow and linear waves is not valid, for example, because the unbalanced flow is strongly nonlinear. This procedure is a rather stringent test of the hypothesis that the mesoscale range is dominated by flow that follows linear wave dynamics. It should be noted that this test is completely agnostic about the spectral slope, which has long been used as the only observational constraint for theories of mesoscale dynamics.

3. Wave energy diagnostics near the tropopause

The wave–vortex decomposition method in Böhler et al. (2014) was developed for a random flow in a linear Boussinesq system with vertically homogeneous statistics. This implies that the vertical structure of the inertia–gravity waves has to be a sum of mutually uncorrelated plane waves with constant vertical wavenumbers and amplitudes. This includes the usual WKB regime of slowly varying wave trains, but it does not describe the atmospheric conditions in the vicinity of the tropopause. Hence, the impact on the wave–vortex decomposition method of vertical inhomogeneity near the tropopause should be carefully considered.²

First, there is the decay of the basic density $\rho_0(z)$ with altitude and the concomitant growth of the wave amplitudes such that Eliassen–Palm flux components like the phase average of $\rho_0 u w$ remain constant. This non-Boussinesq effect means that the usually reported wave energy spectra per unit mass, which are proportional to u^2 and so on, are biased toward the high-altitude tracks, along which $\rho_0(z)$ is lower. For flight tracks spread out over a vertical distance of 3 km or so, we found that, while this effect does not change the results qualitatively, it is a quantitatively noticeable effect. In this paper, we therefore consider only density-weighted energy spectra, as defined in (1) and (18). This eliminates the density decay effect from the observations quite satisfactorily.

Second, there is the presence of a tropopause, where the buoyancy frequency N increases sharply from

² Other effects violating the vertical homogeneity assumption, for example, strong vertical shear, are not discussed here and should be explored in future work.

tropospheric to stratospheric values. This does not affect the Helmholtz decomposition in section 2a, which is insensitive to vertical structure, but it does affect the wave–vortex decomposition in section 2b, which uses the energy equipartition results in (20) or (21) that rely on the vertical homogeneity assumption. So this requires a more detailed analysis, as the physical situation is quite complex. For the wave theory near the tropopause, we will use the Boussinesq equations, in which ρ_0 is taken as constant, but our results carry over to variable $\rho_0(z)$. The theoretical modeling results do not answer all questions as of yet, but they do aid and inform our subsequent analysis of the flight track data in sections 4–6. The trustful reader interested primarily in the data and the differences between the datasets can skip ahead to sections 4.

a. Sharp tropopause model and energy jump

The simplest tropopause model is a jump discontinuity in buoyancy frequency N . Specifically, we let the undisturbed tropopause be at $z = 0$, where it separates tropospheric air in $z < 0$ with buoyancy frequency N_1 from stratospheric air in $z > 0$ with $N_2 > N_1$. The density is continuous at the tropopause, so there are no vortex sheets, and hence the velocity fields are all continuous there. The same is not true, however, for the buoyancy field b , and this obviously affects the energy density on both sides of the tropopause, which in linear Boussinesq theory is

$$E = \frac{\rho_0}{2} \left(u^2 + v^2 + w^2 + \frac{b^2}{N^2} \right). \quad (23)$$

At the tropopause, the velocities are continuous, and so is the vertical material displacement ζ , which is related to the buoyancy by $b = -\zeta N^2$. It follows that the potential energy density term in (23) is proportional to $\rho_0 \zeta^2 N^2$ and hence discontinuous directly at the tropopause, with the resultant jump

$$E(0^+) - E(0^-) = \frac{\rho_0}{2} \zeta^2 (N_2^2 - N_1^2) \quad (24)$$

across the tropopause. This general fact holds both for waves and quasigeostrophic flows. It implies that, *directly at a sharp tropopause*, the energy density is always higher on the stratospheric side ($z = 0^+$) than on the tropospheric side ($z = 0^-$). Of course, this jump would not necessarily show up in aircraft data, because flight tracks are spread out over some altitude range, and in the troposphere this affects the average energies that are sampled along them. We will demonstrate this in a simple model for the inertia–gravity wave structure near the tropopause.

b. Reflection and transmission of inertia–gravity waves

We consider the textbook problem of inertia–gravity waves that are created by tropospheric sources below the region of interest and which subsequently encounter partial reflection and transmission at a sharp tropopause. Arguably, this is the simplest relevant wave model for the case at hand. It results in a stratospheric wave field that consists of upward-propagating transmitted waves, while the tropospheric wave field consists of a correlated superposition of upward incident and downward reflected waves. Hence, in this scenario, the stratospheric wave field is still vertically homogeneous, but not the tropospheric wave field, for which interference of correlated wave modes leads to wave spectra that depend on the distance to the tropopause.

To make this precise, we consider a single plane wave with horizontal wavenumber $k > 0$ and frequency $\omega < 0$ that is oriented at an arbitrary angle in the horizontal plane. We choose the x and y coordinates such that the horizontal wavenumbers are $(k, 0)$; there is no assumption that this coordinate system is aligned with the flight track. Notably, for a single plane wave, the Helmholtz decomposition is trivial and explicit: the x velocity u is induced only by a velocity potential and the y velocity v is induced only by a streamfunction.

Let the vertical velocity in the troposphere and stratosphere be

$$\begin{aligned} w_1 &= \text{Re}[e^{i\theta}(Ae^{+im_1z} + Be^{-im_1z})] \quad \text{and} \\ w_2 &= \text{Re}[e^{i\theta}(Ce^{+im_2z})]. \end{aligned} \quad (25)$$

Here, A , B , and C are the amplitudes of the incident, reflected, and transmitted waves, respectively, $\theta = kx - \omega t$, and the vertical wavenumbers m_1 and m_2 are positive numbers with ratio $\alpha = m_2/m_1$. We do not restrict to hydrostatic waves, because there is evidence that, at the highest wavenumbers of the START08 data, non-hydrostatic effects become important. We do, however, ignore f^2 compared to N^2 , so we use the dispersion relation³

$$\frac{m^2 + k^2}{k^2} = \frac{N^2}{\omega^2 - f^2} \quad \Rightarrow \quad \alpha = \frac{m_2}{m_1} = \sqrt{\frac{N_2^2 - \omega^2}{N_1^2 - \omega^2}}. \quad (26)$$

For hydrostatic waves, $\alpha \approx N_2/N_1$; but in general, α exceeds this value and indeed diverges for tropospheric inertia–gravity waves nearing the buoyancy oscillation limit $\omega^2 = N_1^2$.

³ This is equivalent to the full dispersion relation with N^2 instead of $N^2 - f^2$.

The relevant boundary conditions at $z = 0$ are that both w and w_z are continuous there; the latter can be deduced from the continuity of the horizontal velocity together with $u_x + w_z = 0$. Therefore, $A + B = C$ and $m_1(A - B) = m_2C$, which is solved by

$$A = \frac{1 + \alpha}{2}C \quad \text{and} \quad B = \frac{1 - \alpha}{2}C. \quad (27)$$

The other fields are easily worked out using $u_x + w_z = 0$, $b_t + N^2w = 0$, and $v_t + fu = 0$. In the stratosphere, this yields

$$u_2 = \text{Re}\left(-\frac{m_2}{k}Ce^{i\theta + im_2z}\right), \quad (28)$$

$$v_2 = \text{Re}\left(-\frac{m_2}{k}\frac{f}{i\omega}Ce^{i\theta + im_2z}\right), \quad (29)$$

$$w_2 = \text{Re}(Ce^{i\theta + im_2z}), \quad \text{and} \quad (30)$$

$$\frac{b_2}{N_2} = \text{Re}\left(\frac{N_2}{i\omega}Ce^{i\theta + im_2z}\right). \quad (31)$$

The corresponding fields in the troposphere are

$$u_1 = \text{Re}\left\{-\frac{m_1}{k}Ce^{i\theta}[\alpha \cos(m_1z) + i \sin(m_1z)]\right\}, \quad (32)$$

$$v_1 = \text{Re}\left\{-\frac{m_1}{k}\frac{f}{i\omega}Ce^{i\theta}[\alpha \cos(m_1z) + i \sin(m_1z)]\right\}, \quad (33)$$

$$w_1 = \text{Re}\{Ce^{i\theta}[\cos(m_1z) + i\alpha \sin(m_1z)]\}, \quad \text{and} \quad (34)$$

$$\frac{b_1}{N_1} = \text{Re}\left\{\frac{N_1}{i\omega}Ce^{i\theta}[\cos(m_1z) + i\alpha \sin(m_1z)]\right\}. \quad (35)$$

c. Wave energy diagnostics

In the stratosphere, all the quadratic mean fields and the wave energy are constant, and the equipartition statement in (20) holds (i.e., the wave energy is twice the sum of divergent horizontal kinetic energy and the vertical kinetic energy):⁴

$$\begin{aligned} E_2 &= \frac{\rho_0}{2} \left(\overline{u_2^2} + \overline{v_2^2} + \overline{w_2^2} + \frac{\overline{b_2^2}}{N_2^2} \right) = \rho_0(\overline{u_2^2} + \overline{w_2^2}) \\ &= \rho_0 \frac{m_2^2 + k^2}{k^2} \frac{|C|^2}{2} = \rho_0 \frac{N_2^2}{\omega^2 - f^2} \frac{|C|^2}{2}, \end{aligned} \quad (36)$$

where the overbar denotes an average over phase θ . In the troposphere, conversely, the quadratic mean fields are oscillatory in z :

$$\overline{u_1^2}(z) = \frac{m_1^2}{k^2} \frac{|C|^2}{2} \left[\frac{\alpha^2 + 1}{2} + \frac{\alpha^2 - 1}{2} \cos(2m_1z) \right], \quad (37)$$

$$\overline{v_1^2}(z) = \frac{f^2 m_1^2}{\omega^2 k^2} \frac{|C|^2}{2} \left[\frac{\alpha^2 + 1}{2} + \frac{\alpha^2 - 1}{2} \cos(2m_1z) \right], \quad (38)$$

$$\overline{w_1^2}(z) = \frac{|C|^2}{2} \left[\frac{\alpha^2 + 1}{2} - \frac{\alpha^2 - 1}{2} \cos(2m_1z) \right], \quad \text{and} \quad (39)$$

$$\frac{\overline{b_1^2}(z)}{N_1^2} = \frac{N_1^2}{\omega^2} \frac{|C|^2}{2} \left[\frac{\alpha^2 + 1}{2} - \frac{\alpha^2 - 1}{2} \cos(2m_1z) \right]. \quad (40)$$

Combining this with (36) yields the tropospheric wave energy

$$\begin{aligned} E_1(z) &= \frac{\rho_0}{2} \left(\overline{u_1^2} + \overline{v_1^2} + \overline{w_1^2} + \frac{\overline{b_1^2}}{N_1^2} \right) \\ &= E_2 \frac{N_1^2}{N_2^2} \left[\frac{\alpha^2 + 1}{2} + \frac{\alpha^2 - 1}{2} \left(\frac{f^2}{\omega^2} - \frac{\omega^2}{N_1^2} \right) \cos(2m_1z) \right]. \end{aligned} \quad (41)$$

This consists of a constant plus an oscillation in z with a frequency-dependent amplitude. Notably, in the popular midfrequency approximation, both ω/N_1 and f/ω are small, and hence the oscillation amplitude is negligible. In this approximation, (41) reduces to

$$E_1(z) \approx E_2 \frac{N_1^2}{N_2^2} \frac{\alpha^2 + 1}{2} = E_2 \frac{r^2 + 1}{2r^2}, \quad \text{where} \quad r = \frac{N_2}{N_1}. \quad (42)$$

This shows that for midfrequency waves the tropospheric wave energy is constant and robustly below the stratospheric wave energy, with a typical ratio $E_1/E_2 = 5/8$ for $r = 2$. Conversely, for low-frequency waves with $\omega \approx f$, (41) reduces to

$$E_1(z) \approx E_2 \left[\frac{r^2 + 1}{2r^2} + \frac{r^2 - 1}{2r^2} \cos(2m_1z) \right]. \quad (43)$$

This oscillates around the midfrequency value and is now continuous at the tropopause [i.e., $E_1(0) = E_2$]. Finally, for high-frequency waves with $\omega \approx N_1$, (41) becomes very sensitive to the precise frequency values because of the divergence of α in (26) in the buoyancy oscillation limit $\omega \rightarrow N_1$. For example, the oscillation amplitude for high-frequency waves is

$$\frac{N_1^2}{N_2^2} \frac{\alpha^2 - 1}{2} = \frac{r^2 - 1}{2r^2(1 - s^2)}, \quad \text{where} \quad s = \frac{\omega}{N_1}. \quad (44)$$

Now, our decomposition method estimates E_1 from the energy equipartition result in (20), which was based on vertically homogeneous waves. This leads to a diagnostic error in the presence of a tropopause. Specifically, we use

⁴In this section we only consider wave fields, so we omit the subscript w .

$$\rho_0(\overline{u_1^2} + \overline{w_1^2}) = E_2 \frac{N_1^2}{N_2^2} \left[\frac{\alpha^2 + 1}{2} + \frac{\alpha^2 - 1}{2} \left(1 - 2 \frac{\omega^2}{N_1^2} \right) \cos(2m_1 z) \right] \quad (45)$$

to estimate $E_1(z)$. This agrees with the correct $E_1(z)$ in (41) in the constant term, but the amplitude of the

oscillation term is different and nonzero even for mid-frequency waves. Specifically, the diagnostic error is

$$\Delta E_1 = \rho_0(\overline{u_1^2} + \overline{w_1^2}) - E_1 = E_2 \frac{N_1^2}{N_2^2} \frac{\alpha^2 - 1}{2} \left(1 - \frac{f^2}{\omega^2} - \frac{\omega^2}{N_1^2} \right) \cos(2m_1 z). \quad (46)$$

For typical values, such as $f/N_1 \approx 0.01$, this expression is equal to its midfrequency approximation for practically all wave frequencies except those within a few percent of either f or N_1 . (This includes high-frequency waves, for which the divergence of α^2 is cancelled by the bracketed term.) Hence, we can replace (46) by

$$\Delta E_1 \approx E_2 \frac{r^2 - 1}{2r^2} \cos(2m_1 z) \quad (47)$$

to excellent approximation. This shows that ΔE_1 increases with $r \geq 1$, but is never more than half of the stratospheric wave energy. Notably, ΔE_1 is positive directly at the tropopause $z = 0$, which means the diagnosed wave energy always exceeds the true wave energy there. Indeed, the diagnosed wave energy may then exceed the total energy of the flow there, which in turn would lead to unphysical negative residual vortex energies diagnosed in (22). Arguably, this plays some role in the analysis of the START08 data in section 5 below.

d. Random-phase averaging over flight tracks

The tropospheric $\cos(2m_1 z)$ oscillations raise the question of how to interpret diagnosed wave energies that are obtained by averaging over flight tracks taken at many different altitudes in the troposphere. Two situations can be envisaged in which uncertainties do not arise. First, the flight tracks could for some hypothetical reason be concentrated in the immediate vicinity below the tropopause $z = 0$ such that $\cos(2m_1 z)$ can be approximated by unity. As pointed out in the last section, in this situation the diagnosed wave energy would always exceed the true wave energy on the tropospheric side of the tropopause. Indeed, the diagnosed wave energy would be continuous across the tropopause such that

$$\rho_0[\overline{u_1^2}(0) + \overline{w_1^2}(0)] = E_2 = \rho_0(\overline{u_2^2} + \overline{w_2^2}). \quad (48)$$

This follows from the continuity of the velocity components at the tropopause. There is no obvious reason,

however, why flight tracks should be accumulated directly below the tropopause.

This leads to the second situation, which is much more practically relevant. Here, averaging over tropospheric flights at random altitudes below the tropopause leads to an effective random-phase average in the vertical of the diagnosed wave energy. The $\cos(2m_1 z)$ terms then average to zero, and the wave-vortex decomposition becomes accurate in terms of the phase-averaged energies. In other words, the phase-averaged diagnostic error ΔE_1 is zero. Of course, the efficacy of such random-phase averaging depends on the number of flight tracks, their altitude range below the tropopause, and the vertical wavelengths that are involved. Basically, for a given vertical wavelength, a large uniformly random sample of flights within at least a quarter wavelength below the tropopause would lead to a diagnosed wave energy equal to

$$\begin{aligned} \langle \rho_0[\overline{u_1^2}(z) + \overline{w_1^2}(z)] \rangle &= \langle E_1(z) \rangle = E_2 \frac{N_1^2}{N_2^2} \frac{\alpha^2 + 1}{2} \\ &= E_2 \frac{r^2 + 1 - 2s^2}{2r^2(1 - s^2)}, \end{aligned} \quad (49)$$

where the angle brackets denote phase averaging. For instance, if the tropospheric flight tracks cover an altitude range of 1.5 km below the tropopause, then this argument predicts that the energy level of waves with a vertical wavelength of 6 km or shorter will be diagnosed at their phase-averaged level given by (49). Presumably, the energy level of waves with larger wavelength would be diagnosed at a partially phase-averaged level, which ranges between (49) and the tropopause limit E_2 in (48). For hydrostatic waves, (49) reduces to the midfrequency expression

$$\begin{aligned} \langle E_1(z) \rangle &= E_2 \frac{r^2 + 1}{2r^2}, \quad \text{such that} \\ \langle E_1(z) \rangle &= E_2 \frac{5}{8} \quad \text{for } r = 2. \end{aligned} \quad (50)$$

On the other hand, for high-frequency waves, $\langle E_1(z) \rangle > E_2$ if $\omega^2 > N_1^2/2$ (i.e., $s^2 > 1/2$). This indicates that the phase-averaged wave energy level in the troposphere is sensitive to the high-frequency content of the wave field. Such high-frequency waves are associated with large horizontal wavenumbers, but presumably this sensitivity is to some extent spread to lower horizontal wavenumbers by the kinematic aliasing inherent in one-dimensional power spectra.

4. MOZAIC data

In this section, we describe the application of the decomposition method to the MOZAIC data, split into lower stratosphere and upper troposphere. We use the same set of flights from 2002 to 2010 as in Callies et al. (2014) but apply different selection criteria to separate flight segments into stratospheric and tropospheric. We restrict all data to the northern midlatitudes (30°–60° latitude) and to above 350 hPa to exclude takeoff and landing. Rare velocity spikes are removed by dismissing data that changes by more than 10 m s^{-1} from one data point to the next (separated by about 1 km). Within the remaining data, we select segments of nearly constant altitude by introducing break points where the seven-point running mean of altitude changes by more than 3 m from one point to the next. This reliably identifies segments of very nearly constant altitude while ignoring small-scale variations that presumably are due to up- and downdrafts experienced by the aircraft. For each segment, the data are rotated into a coordinate system aligned with the best-fit great circle. We retain only segments that are at least 250 km long, have an average spacing of at most 1.2 km, and deviate from the best-fit great circle by less than 0.1° .

For the segments passing these criteria, the ERA-Interim (Dee et al. 2011) is consulted to classify them as tropospheric or stratospheric. For each data point, we compute the stratification at flight altitude from the reanalysis profile located closest in space and time to the data point. A segment is classified as “tropospheric” if the buoyancy frequency (square root of the segment-average stratification) is less than $N = 1.2 \times 10^{-2} \text{ s}^{-1}$ and as “stratospheric” if it is greater than $N = 1.8 \times 10^{-2} \text{ s}^{-1}$; segments that fit neither of these categories are discarded to exclude segments that cross the tropopause. This results in a total of 2752 tropospheric and 4681 stratospheric segments.⁵ We base the classification into

tropospheric and stratospheric on reanalysis rather than ozone concentration (Lindborg 2015), because not all MOZAIC flights have complete ozone data. This difference in classification has no noticeable effect on the results.

Wavenumber spectra are estimated by applying a Hann window and computing a discrete Fourier transform for each segment, assuming a spacing equal to the average spacing over the segment.⁶ The squared Fourier amplitudes are averaged over the segments and over wavenumber bins uniformly partitioning the logarithmic wavenumber space with 10 bins per decade.

The resulting spectra for the upper troposphere and lower stratosphere both exhibit the transition from steep spectra at synoptic scales to flatter spectra at mesoscales (Figs. 2a,b). This transition from a spectral slope of about -3 and one of about $-5/3$ occurs at wavelengths around 200 km in the troposphere and around 500 km in the stratosphere. At scales smaller than $k = 2\pi/10 \text{ km}$, the spectra flatten again and become nearly white. This indicates the dominance of measurement noise and errors associated with the rounding in the reported locations, velocities, and temperatures. We therefore disregard these small scales in the following analysis.

The Helmholtz decomposition of the horizontal kinetic energy spectrum shows a dominance of the rotational component at synoptic scales and a divergent component that becomes appreciable at the transition to mesoscales, both in the troposphere and the stratosphere (Figs. 2c,d). The ratio of the divergent to the rotational component in the mesoscale range, however, differs between the troposphere and the stratosphere. In the troposphere, the rotational component is larger than the divergent component over the entire mesoscale range. In the stratosphere, conversely, the divergent component dominates over the rotational component by about a factor of 2. This is consistent with the tendency diagnosed by Lindborg (2015) that there is more rotational energy in the mesoscale range in the upper troposphere than in the lower stratosphere. But the ratios between the divergent and rotational energy spectra at mesoscale wavenumbers are larger than the ratios between Lindborg’s structure functions at mesoscale separations, because the mesoscale spectra are not contaminated by leakage of synoptic-scale rotational energy (see the appendix).

⁵Note that the number of segments passing the selection criteria is much larger here than in Callies et al. (2014) (cf. Fig. 1), because here we require segments to be only 250 km long instead of 6000 km long.

⁶In contrast to Callies et al. (2014), no interpolation onto a regular grid is attempted, because the locations are reported only to an accuracy of 0.01° in longitude and latitude. The two approaches give indistinguishable results at scales used for the analysis.

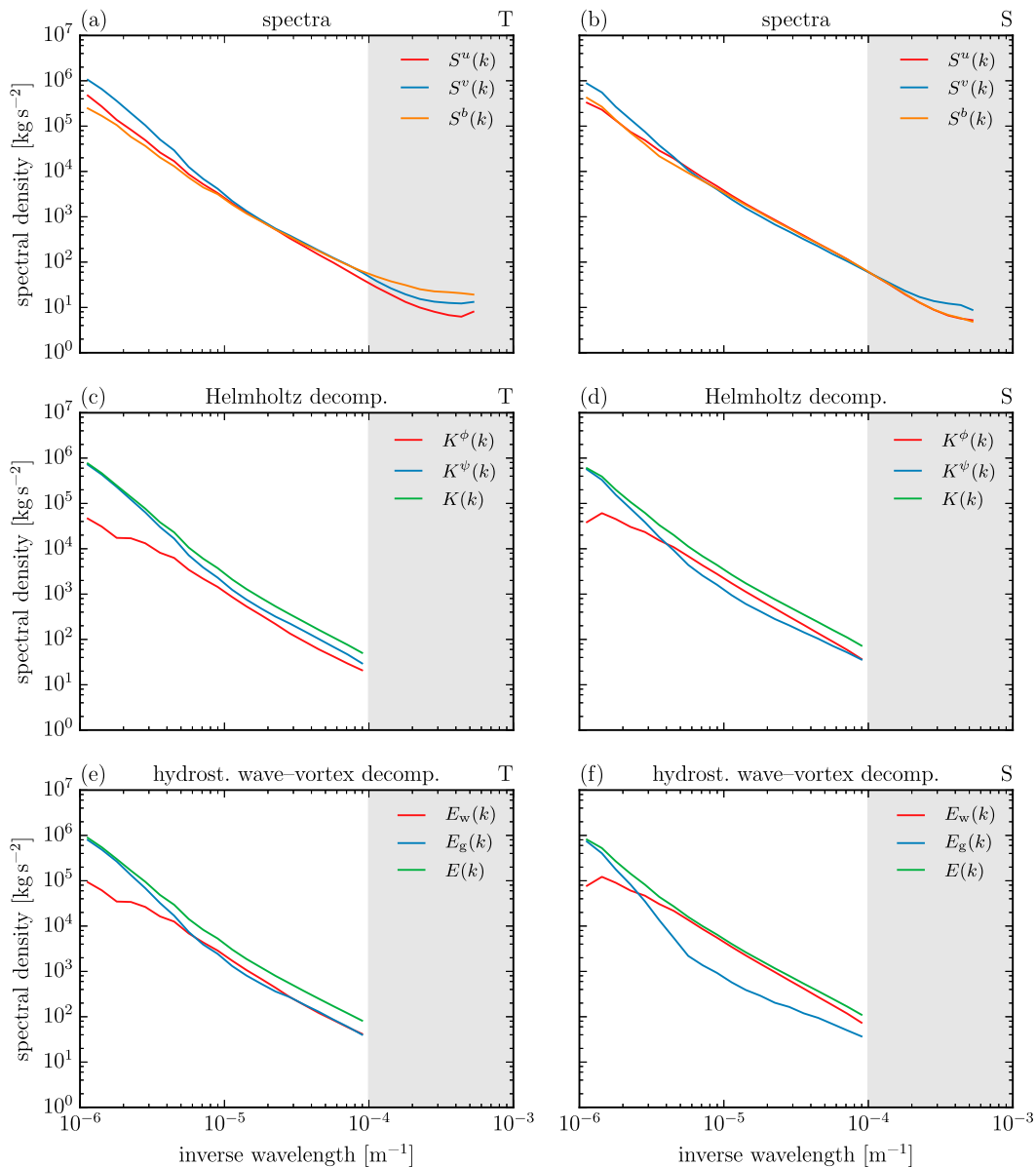


FIG. 2. Wavenumber spectra from the MOZAIC data, split into (left) the upper troposphere and (right) the lower stratosphere. Shown are (a),(b) the raw spectra, (c),(d) the Helmholtz decomposition, and (e),(f) the hydrostatic wave–vortex decomposition. The raw spectra include a shaded region of unreliable small-scale data below 10-km wavelength, which is not used in the subsequent analysis.

This Helmholtz decomposition shows that the mesoscale MOZAIC data in the upper troposphere cannot be explained by inertia–gravity waves alone, because linear wave theory predicts that the divergent component of kinetic energy is at least as large as the rotational component. In the lower stratosphere, on the other hand, where the divergent component dominates, inertia–gravity waves are a plausible explanation for the data. These two results will be confirmed below with the wave–vortex decomposition. It should

be noted, however, that the Helmholtz decomposition is independent of any vertical homogeneity assumption that will be necessary for the wave–vortex decomposition.

To apply the wave–vortex decomposition in the upper troposphere, we need to assess the amount of random-phase averaging due to the distribution of flight altitudes with respect to the tropopause. To do this quantitatively, we would need an estimate for the vertical wavelength of tropospheric waves. Such an estimate is not available

directly from the data, but a vertical wavelength much smaller than the horizontal wavelength is expected for hydrostatic inertia–gravity waves. The START08 data discussed below support that waves are sufficiently hydrostatic at the horizontal scales resolved by the MOZAIC data. Given that only a quarter of the vertical wavelength must be sampled and that the tropospheric flight altitudes vary by some 1.5 km (two standard deviations), it can be expected that at least some degree of random-phase averaging occurs, which will reduce the diagnostic error below the maximal error $\Delta E_1(0)/E_2 = (r^2 - 1)/2r^2 = 0.375$ for a typical $r = N_2/N_1 = 2$. Further reduction of the diagnostic error in (46) can be expected if the wave frequencies approach the inertial frequency at large horizontal scales. Together, these two effects likely render the wave–vortex decomposition relatively robust also in the upper troposphere.

The wave–vortex decomposition corroborates the differences in mesoscale characteristics in the upper troposphere and lower stratosphere that were diagnosed by the Helmholtz decomposition (Figs. 2e,f). In the lower stratosphere, the same result is obtained as in Callies et al. (2014): the diagnosed total wave energy nearly matches the observed total energy across the mesoscale range. The picture differs significantly in the upper troposphere, where the wave–vortex decomposition attributes no more than two-thirds of the total energy to the wave component. This indicates that the observed mesoscale flow is inconsistent with the dispersion and polarization relations of inertia–gravity waves, as already suggested by the dominance of the rotational component of kinetic energy.

It is useful to test a second prediction of linear wave dynamics, particularly because in the upper troposphere the wave–vortex decomposition result is contradicted by the START08 dataset, as discussed below. As such an independent test, which is based on a different set of assumptions, we consider the ratio between the tropospheric and stratospheric total energy spectra $E_1(k)/E_2(k)$, where the subscripts 1 and 2 denote the tropospheric and stratospheric spectra, respectively. For hydrostatic waves ($s = 0$), complete random-phase averaging, and $r = 2$, (49) predicts this ratio to be 0.625. Across the resolved mesoscale range (10–200 km), the observed ratio roughly matches this prediction (Fig. 3a). So even though the wave–vortex decomposition indicates that the tropospheric observations are inconsistent with linear waves, the ratio between the tropospheric and stratospheric total energies is consistent with the simple model of partially reflecting upward-propagating inertia–gravity waves discussed in section 3. We will see in the following section that the

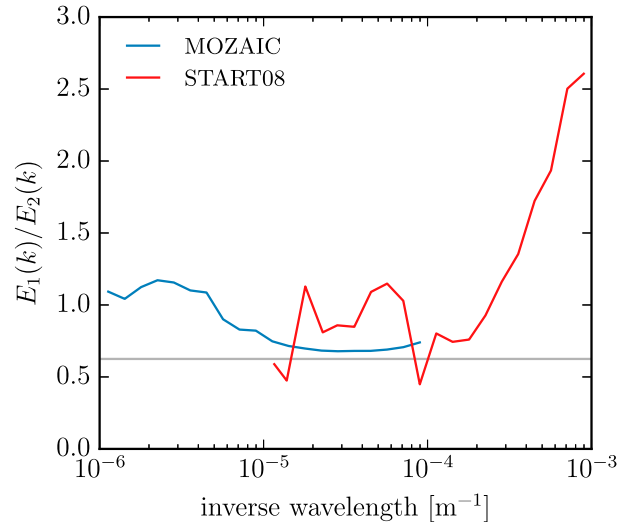


FIG. 3. Ratios of the tropospheric and stratospheric total energy spectra for the MOZAIC and START08 data. The horizontal line is the theoretical prediction for phase-averaged hydrostatic wave energies in (50) with $r = 2$.

START08 data offer additional support for the inertia–gravity wave hypothesis.

5. START08 data

As part of the START08 campaign (Pan et al. 2010; Zhang et al. 2015), all three components of the wind vector, as well as standard meteorological variables like temperature and pressure, were measured aboard the NSF/NCAR Gulfstream V (GV) research aircraft. These are targeted observations of mesoscale variability performed with high-precision, well-calibrated instruments, which builds our confidence in the quality of the data.

All START08 data used in our analysis are located over the continental United States and Canada (Fig. 4). We identified a total of 15 upper-tropospheric segments and 65 lower-stratospheric segments that were straight and at least 100 km long. The classification into tropospheric and stratospheric was done by inspecting along-track–altitude sections of stratification from reanalysis. Only tropospheric segments above 350 hPa are used to facilitate the comparison to the upper-tropospheric data from MOZAIC and to obtain relatively homogeneous statistics. Spectra are computed the same way as described above for the MOZAIC data. The only difference is the range of wavenumbers considered, which is here chosen to extend from $k = 2\pi/100$ km to $k = 2\pi/1$ km, because the flight segments are shorter, location is reported with higher precision, and the 1 Hz sampling interval amounts to a spacing of about 200–250 m.

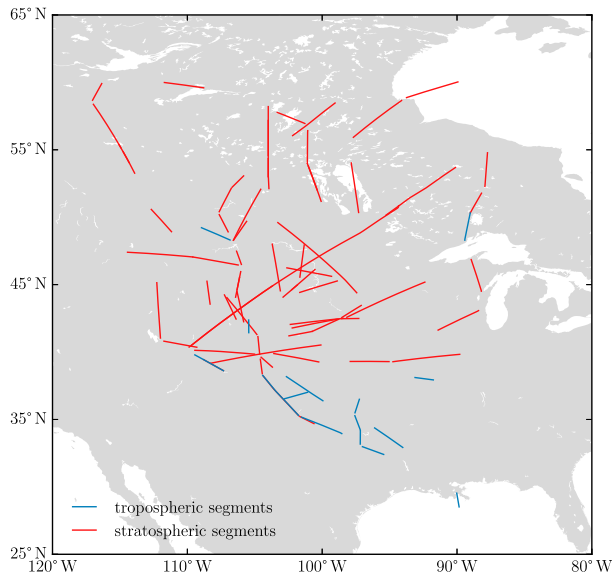


FIG. 4. Map of the START08 segments used to compute the wavenumber spectra for the upper troposphere (blue) and lower stratosphere (red).

The scales at which the spectra can be accurately estimated are too small to resolve the synoptic-to-mesoscale transition. The tropospheric horizontal kinetic energy spectrum $K(k)$ has a slope of roughly $-5/3$ at wavelengths of 10–100 km and of roughly -2 at wavelengths of 1–10 km (Fig. 5; Table 1). The spectra $S^u(k)$, $S^v(k)$, and $S^b(k)$ have roughly the same magnitude and shape over the entire range of scales. The vertical velocity spectrum $S^w(k)$ is significantly smaller except at scales smaller than $k = 2\pi/3$ km, where $S^w(k)$ has about the same magnitude as the other spectra.

The stratospheric horizontal kinetic energy spectrum $K(k)$ also has a slope of roughly $-5/3$ at wavelengths of 10–100 km but transitions to a significantly larger slope of -2.6 at wavelengths of 1–10 km (Fig. 5; Table 1; cf. Bacmeister et al. 1996; Zhang et al. 2015). Again, $S^u(k)$, $S^v(k)$, and $S^b(k)$ have roughly the same magnitude and shape over the entire range of scales. The vertical velocity spectrum $S^w(k)$ is much smaller than the other spectra at wavelengths of 10–100 km and is of the same order but somewhat smaller at wavelengths of 1–10 km.

The change in spectral slope in the lower stratosphere is inconsistent with the hypothesis that mesoscale dynamics are governed by stratified turbulence. This theory requires the energy spectra to follow a $k^{-5/3}$ power law all the way down to the much smaller dissipation scales (Lindborg 2006). We will test whether the START08 data are instead consistent with linear inertia-gravity waves using—as above for the MOZAIC data—the Helmholtz and wave-vortex decompositions

plus the ratio between the total energy spectra in the upper troposphere and lower stratosphere.

The Helmholtz decomposition shows that the horizontal kinetic energy has a significant divergent component over the entire range of resolved scales, in both the lower stratosphere and the upper troposphere (Figs. 5c,d). In the lower stratosphere, the rotational and divergent components are about equal, with a slight dominance of the divergent component at wavenumbers around $k = 2\pi/50$ km. In the upper troposphere, the divergent component is significantly larger than the rotational component at scales larger than $k = 2\pi/5$ km. At smaller scales, the two components converge.

Wavelengths of 10–100 km are resolved by both the START08 and the MOZAIC data. In this overlap, the Helmholtz decompositions in the lower stratosphere are very similar (Figs. 2d, 5d). In the upper troposphere, however, the START08 data yield a significant dominance of the divergent component (Fig. 5c), while the MOZAIC data yield a significant dominance of the rotational component (Fig. 2c). This means that the START08 data allow the inertia-gravity wave interpretation, while the MOZAIC data seem to exclude it in the upper troposphere.

We next perform the wave-vortex decomposition, assuming there is sufficient random-phase averaging in the upper troposphere. The statistics are less robust here than for the MOZAIC data, because there are only 15 tropospheric segments. These segments are fairly well distributed in altitude, however, which effects at least some degree of phase averaging. If there were no phase averaging, the maximum relative diagnostic error would be again a modest $\Delta E_1(0)/E_2 = (r^2 - 1)/2r^2 = 0.375$. The phase averaging that does occur presumably reduces this diagnostic error significantly.

The wave-vortex decomposition yields a good match between the diagnosed total wave energy and the observed total energy across the resolved scales and in both the upper troposphere and lower stratosphere (Figs. 5e–h). We perform both the hydrostatic decomposition given by (21) and the nonhydrostatic version given by (20), which takes advantage of the vertical velocity observations. There are slight improvements in the match between the observed and diagnosed energies at scales smaller than $k = 2\pi/10$ km. This indicates that nonhydrostatic effects become appreciable at these small scales.

The START08 wave-vortex decomposition is consistent with the MOZAIC data in the lower stratosphere, where mesoscale observations from both datasets are compatible with the dispersion and polarization relations of linear inertia-gravity waves. As

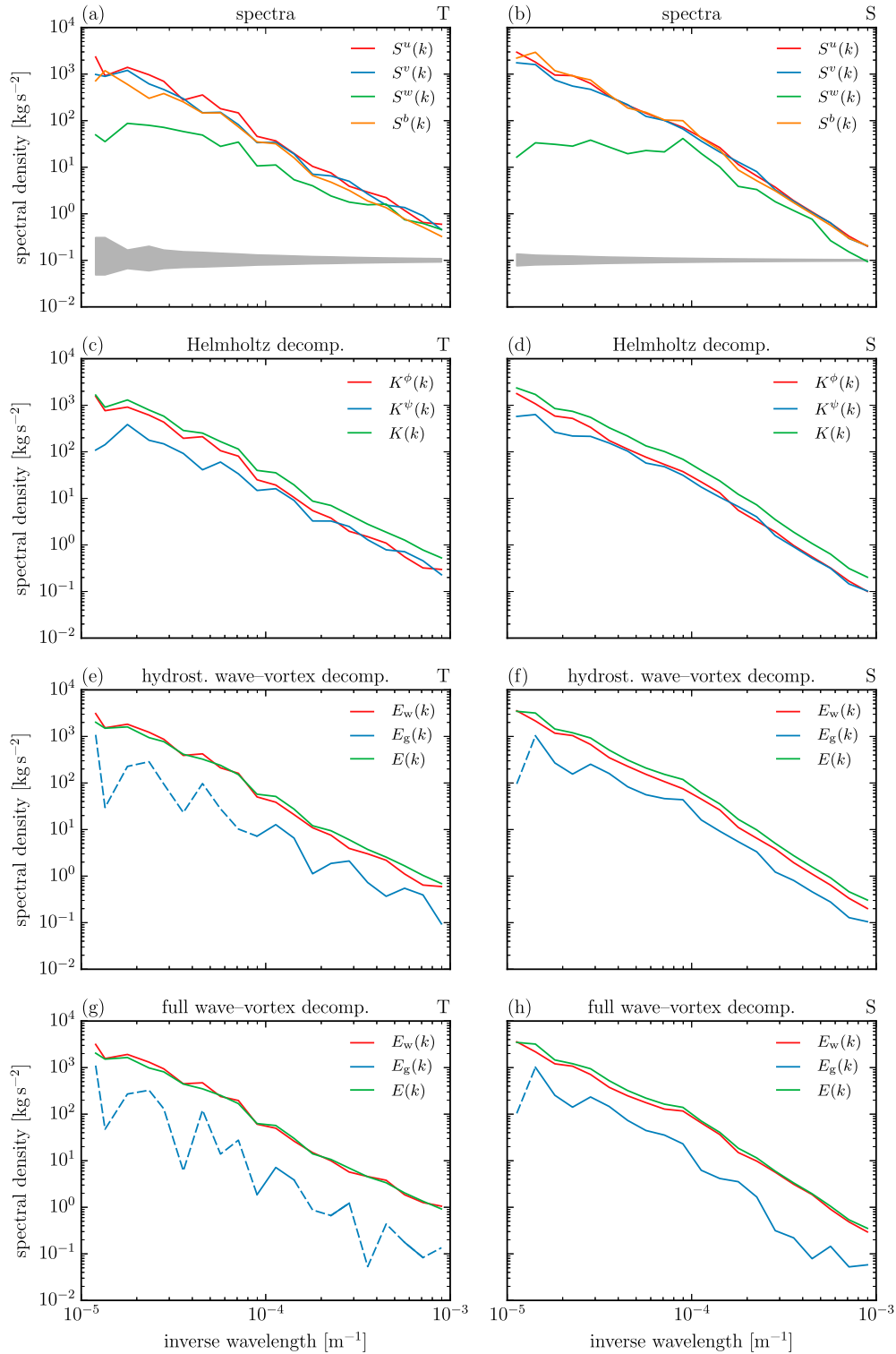


FIG. 5. Wavenumber spectra from the START08 data for the (left) upper troposphere and (right) lower stratosphere. Shown are (a),(b) the raw spectra, (c),(d) the Helmholtz decomposition, (e),(f) the hydrostatic wave-vortex decomposition, and (g),(h) the full nonhydrostatic wave-vortex decomposition. Additionally, the absolute value of the diagnosed vortex energy is plotted in dashed lines to show the energy's magnitude where it turns negative.

TABLE 1. Spectral slopes of START08 horizontal kinetic energy spectra $K(k)$ as measured by least-squares fits over the stated wavelength range (fits performed in logarithmic space).

	10–100 km	1–10 km
Troposphere	–1.64	–1.96
Stratosphere	–1.71	–2.60

for the Helmholtz decomposition, however, the two datasets differ in the upper troposphere: the START08 wave–vortex decomposition contradicts that of the MOZAIC data. The START08 data are consistent with inertia–gravity waves over the entire observed range, while the MOZAIC data show a much larger rotational component at mesoscales and are thus incompatible with the inertia–gravity interpretation. The source of this mismatch will be explored in the next section.

Before discussing that, however, we compare the observed ratio of the total energy between the upper troposphere and lower stratosphere with that predicted by the wave model described in section 3. The observed energies in the upper troposphere and lower stratosphere are roughly equal for 4–100-km wavelengths (Fig. 3b). At smaller scales, the stratospheric energy drops below the tropospheric one, owing to the steeper slope in the stratospheric spectra.

The predicted ratio for a monochromatic wave in the hydrostatic limit is 0.625 if complete phase averaging occurs. For higher-frequency waves, the ratio increases, crosses unity at $\omega^2 = N_1^2/2$, and diverges in the nonhydrostatic limit. If there is no phase averaging, a ratio between 0.625 (nonrotating limit) and 1 (inertial limit) is predicted.

To get a sense for the wave frequencies, we consider $S^w(k)/S^b(k)$. This ratio equals ω^2/N^2 for monochromatic waves; for a broadband wave field, the estimated frequency is an average over the collection of waves. In both upper troposphere and lower stratosphere, the observations show that $S^w(k) \ll S^b(k)$ for scales larger than about $k = 2\pi/10$ km, indicating that waves at these scales are in the hydrostatic limit (Fig. 6). At smaller scales, $S^w(k)$ is of the same order as $S^b(k)$, so waves are significantly nonhydrostatic. In the upper troposphere, $S^w(k)/S^b(k)$ slightly exceeds unity for the smallest resolved scales, which is not possible for linear waves that are confined to $\omega^2 < N_1^2$. There is considerable uncertainty in the estimated ratio, however, and it is not clear whether this result is significant.

For scales larger than about $k = 2\pi/30$ km, the diagnosed frequencies in the upper troposphere and lower stratosphere roughly match and indicate that waves at these scales are in the hydrostatic limit (Fig. 6). The observed match of the total energy spectra at these scales is thus broadly consistent with the predicted

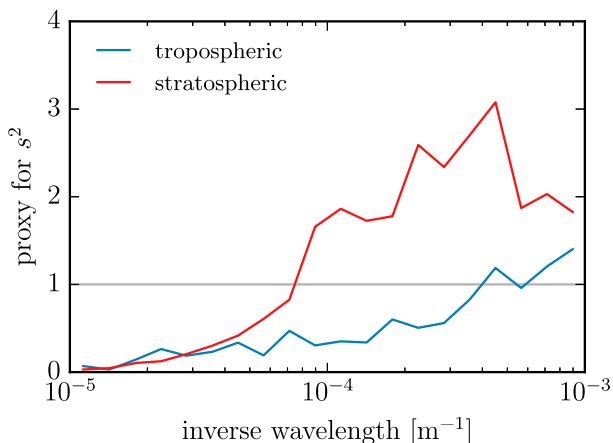


FIG. 6. Tropospheric ratio $S^w(k)/S^b(k)$ and stratospheric ratio $N_2^2 S^w(k)/N_1^2 S^b(k)$ as proxies for $s^2 = \omega^2/N_1^2$ from the START08 data, assuming a monochromatic wave field.

values (Fig. 3). The observed ratio is somewhat larger than the 0.625 predicted for full random-phase averaging with $r = 2$, but it is consistent with the predicted range if there is little phase averaging.

At scales smaller than $k = 2\pi/30$ km, the diagnosed frequencies differ in the upper troposphere and lower stratosphere (Fig. 6). The stratospheric frequencies exceed the largest allowable frequency in the troposphere, $\omega^2 > N_1^2$, potentially defying the simple picture of waves propagating upward from the troposphere. Wave sources might be present aloft. The mismatch of tropospheric and stratospheric frequencies furthermore discourages the application of our monochromatic prediction of the energy ratio. It is interesting to note, however, that the dominance of the tropospheric energy at the smallest scales is consistent with the predictions from phase averaging in the nonhydrostatic regime of (50). These are the scales at which nonhydrostatic effects are strong (Fig. 6).

In summary, the START08 data are consistent with the wave hypothesis, with the strongest indication coming from the successful wave–vortex decomposition. In the lower stratosphere, this diagnosis is consistent with the MOZAIC data, but in the upper troposphere, it is not. We explore the source of this inconsistency between the two datasets in the next section. For small scales, the START08 data suggest that the wave field may not exclusively consist of waves propagating up from sources below the upper troposphere.

6. Comparison of datasets

The two datasets both cover the wavelengths from 10 to 100 km. In this section, we use this range of overlap to discuss the discrepancies between the two datasets that

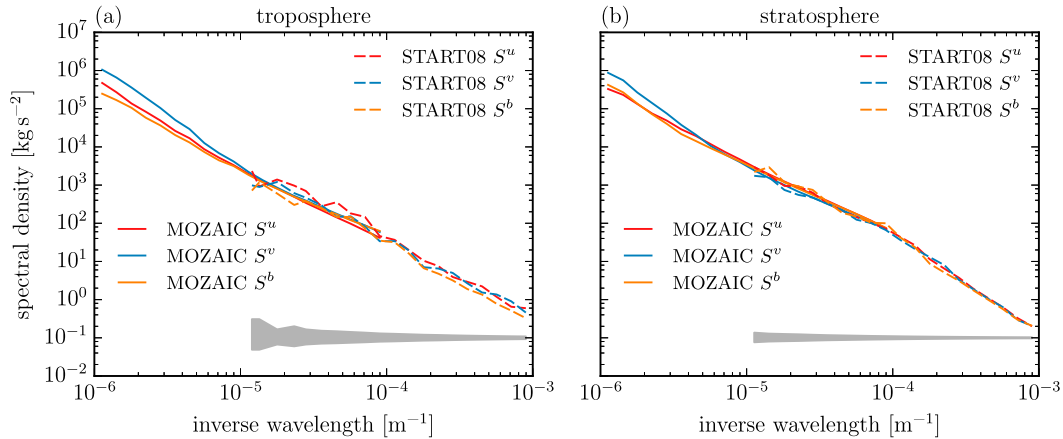


FIG. 7. Comparison of (a) tropospheric and (b) stratospheric wavenumber spectra from MOZAIC (solid) and START08 (dashed). The 95% confidence intervals for the START08 data are shown by the gray shading. No confidence interval is given for the MOZAIC data, because the large number of segments renders it imperceptibly small.

became apparent in the wave–vortex decomposition presented above. We here compare directly the spectra $S^u(k)$, $S^v(k)$, and $S^b(k)$ so that this comparison is independent of the various assumptions used in the analysis above.

In the lower stratosphere, all three spectra match remarkably well in the range of overlap (Fig. 7b). This explains the consistency of the results for the stratosphere. In the upper troposphere, however, discrepancies arise (Fig. 7a). While $S^v(k)$ and $S^b(k)$ roughly match in the range of overlap, $S^u(k)$ is significantly larger in the START08 data than in the MOZAIC data. It can be seen directly from (15) and (16) that this leads to the diagnosis of a reduced divergent component of kinetic energy in the MOZAIC data and subsequently to the difference in interpretation laid out in the previous two sections.

The uncertainty in the tropospheric START08 data is relatively large, because only 15 segments are available. It is unlikely, however, that the persistently elevated START08 $S^u(k)$ over the range of overlap can be attributed to random effects. If the discrepancy was random, there would be about an equal number of wavenumbers at which the START08 $S^u(k)$ is larger and smaller than the MOZAIC $S^u(k)$, which is not the case. Furthermore, the START08 data are qualitatively consistent with spectra computed from GV data from the 2006 T-REX and the 2014 Deep Propagating Gravity Wave Experiment over New Zealand (DEEPWAVE) campaigns. These are not shown, because they have an even more limited number of segments in the upper troposphere and therefore poor statistics. But these results do increase the confidence in the robustness of the START08 results.

The next possible explanation for the mismatch is that the two datasets sample distinct tropospheric conditions. We performed a number of tests to check whether the inconsistency is due to spatial or temporal variations in mesoscale characteristics. We restricted the MOZAIC data in space to a sector over continental North America and in time to the months of the START08 campaign (April–June), but the inconsistency with the START08 data is robust. While there is a difference in mesoscale energy levels between land and ocean (cf. Nastrom et al. 1987), the MOZAIC data always exhibit a low $S^u(k)$, leading to a dominance of the rotational component of kinetic energy in the upper troposphere. We also did not find any bias due to flight-track orientation, neither relative to cardinal direction nor relative to the segment-average wind. New data from the MOZAIC sequel In-Service Aircraft for a Global Observing System (IAGOS) shows the same behavior.

Having ruled out these sources for the inconsistencies, it seems likely that they stem from the difference in instrumentation and data processing. The confidence in the GV data collected in the START08 campaign is high, because the instrumentation was developed and calibrated specifically to target mesoscale variability.⁷ An in-depth comparison of the

⁷ Zhang et al. (2015) recently raised concerns about the accuracy of GV wind measurements at scales smaller than $k = 2\pi/10$ km. The overlap with the MOZAIC data does not extend to such small scales, however, so this potential issue does not affect our diagnosis of the inconsistency. The consistency with inertia–gravity waves at scales smaller than $k = 2\pi/10$ km is surprising, if measurement error dominated on these scales, but the results at the smallest scales should be taken with a grain of salt.

MOZAIC data to those collected with dedicated research aircraft would be useful to reconcile these two datasets. Such an investigation should also explore whether the targeting of specific mesoscale conditions by START08 (Pan et al. 2010) introduces any bias that leads to the mismatch.

7. Summary and conclusions

The observations of mesoscale variability are consistent with inertia–gravity waves in the lower stratosphere. Two datasets, the MOZAIC data collected aboard commercial aircraft and the START08 data collected with the NSF/NCAR GV research aircraft, agree in their diagnosis that the relative magnitudes of mesoscale along-track velocity, across-track velocity, and buoyancy variations are consistent with the dispersion and polarization relations of inertia–gravity waves. It should be noted that this result is not inconsistent with a dominance of mesoscale structure functions by their rotational component (Lindborg 2015), because structure functions suffer from the alias of synoptic-scale rotational energy into mesoscale separations (see the appendix). Furthermore, a steepening of the observed spectra at scales smaller than $k = 2\pi/10$ km is at odds with the alternative explanation of mesoscale variability with stratified turbulence theory. The observations contradict this theory's prediction that the spectral slope is $-5/3$ all the way down to dissipation scales.

It is important to note that power-law spectra do not necessarily imply strongly nonlinear cascade dynamics. It is known that weak interactions between quasi-linear waves can lead to power-law spectra (e.g., McComas and Müller 1981; Polzin and Lvov 2011), and other explanations consistent with quasi-linear waves are possible: for example, weak interaction with the balanced component of the flow. How such weakly nonlinear dynamics may shape the mesoscale energy spectrum is largely unexplored. The wave interpretation is thus not inconsistent with the observed power-law spectra and the change in spectral slope, but an explanation for the spectral shape is so far missing.

The wave–vortex decomposition used to test the signal's consistency with inertia–gravity waves relies on the assumption of vertical homogeneity. Because of the presence of the tropopause, this assumption may break down in the upper troposphere. We showed, however, that if flights sample the upper troposphere at sufficiently variable altitudes, random-phase averaging occurs and renders the decomposition robust. Other possible violations of the assumptions have not been discussed: for example, the presence of strong vertical

shear or horizontal anisotropy. These should be explored in future work.

The results obtained from the wave–vortex decomposition in the upper troposphere differ between the two datasets. The START08 data are consistent with inertia–gravity waves dominating mesoscale variability. In contrast, the MOZAIC data imply a larger rotational component of kinetic energy and are thus inconsistent with inertia–gravity waves. The discrepancy between the two datasets in the upper troposphere can be traced to decreased mesoscale variability in the along-track wind in the MOZAIC data.

The high confidence in the START08 data suggests that the inertia–gravity wave interpretation also applies for the upper troposphere. This result should be confirmed with more tropospheric observations that yield better statistics. It is also hoped that the START08 and MOZAIC datasets can be reconciled by checking the MOZAIC data against the highly accurate instruments of the GV.

We also compared the observed ratio between the total tropospheric and stratospheric energy spectra with predictions from a simple model of upward-propagating waves that are partially reflected at the tropopause. Both the MOZAIC and START08 data are roughly consistent with the predicted ratio at 10–100 km. At smaller scales, the START08 data suggest different frequency contents in the troposphere and stratosphere, barring the application of the monochromatic wave model. The data also show that stratospheric wave frequencies may exceed those allowed in the troposphere.

Another avenue for progress in understanding the mesoscale dynamics is to build on work with numerical models that resolve the mesoscale range (e.g., Hamilton et al. 2008; Skamarock et al. 2014; Bierdel et al. 2016). These models have been shown to compare favorably against observations and could be used to more extensively explore the dynamics of mesoscale flows. Instead of the keyhole view of atmospheric flow available from one-dimensional aircraft observations, models deliver the full time-varying three-dimensional flow field and thus allow a direct test of whether mesoscale winds are consistent with quasi-linear wave dynamics.

Acknowledgments. We thank Fuqing Zhang for giving us access to the START08 data. Valuable feedback from Peter Bartello, Chris Snyder, and an anonymous reviewer are gratefully acknowledged. Financial support for JC and RF came from the U.S. National Science Foundation under Grant OCE-1233832 and for OB from the U.S. National Science Foundation under

Grants DMS-1516324 and DMS-1312159 as well as from the U.S. Office of Naval Research under Grant 141512355.

APPENDIX

A Decomposition of Spectra and Structure Functions

Structure functions are a common tool for characterizing the statistics of turbulent flows (e.g., [Batchelor 1953](#)). For some variable a , the (second order) structure function at separation r is defined as

$$\Delta^a(r) = \langle \rho_0 [a(x+r) - a(x)]^2 \rangle, \quad (\text{A1})$$

where x is the along-track coordinate. The structure function is related to the power spectrum $S^a(k)$ by^{A1}

$$\Delta^a(r) = 2 \int_{-\infty}^{\infty} S^a(k) [1 - \cos(kr)] dk. \quad (\text{A2})$$

The structure function thus contains the same information as the power spectrum. One must be cautious when interpreting structure functions, however, because the structure function at some separation r is not necessarily reflective of variability at that scale (e.g., [Babiano et al. 1985](#)). For a power-law spectrum $S^a(k) \sim k^{-n}$, the structure function is only representative of the spectrum near $k = r^{-1}$ if $1 < n < 3$. If the spectrum is steeper ($n > 3$), the relation is nonlocal: the structure function at separation r is dominated by variability at scales larger than $k = r^{-1}$. In this case, the structure function saturates at r^2 .

This point is illustrated in [Fig. A1](#), showing the integrand of [\(A2\)](#) for two power-law spectra, one with $n = 5/3$ and one with $n = 3$. This shows the contributions to the structure function at separation $r = k^{-1}$. For $n = 5/3$, the contribution is localized at wavenumbers somewhat larger than $k = r^{-1}$, so the structure function is spectrally local. For $n = 3$, however, all wavenumbers $k \ll r^{-1}$ contribute equally to the structure function at separation r , so the structure function is spectrally nonlocal. This is important to keep in mind when interpreting the structure functions computed from aircraft data, as shown in the following.

We now show that the data analyzed in [Callies et al. \(2014\)](#) yield structure functions that at mesoscale

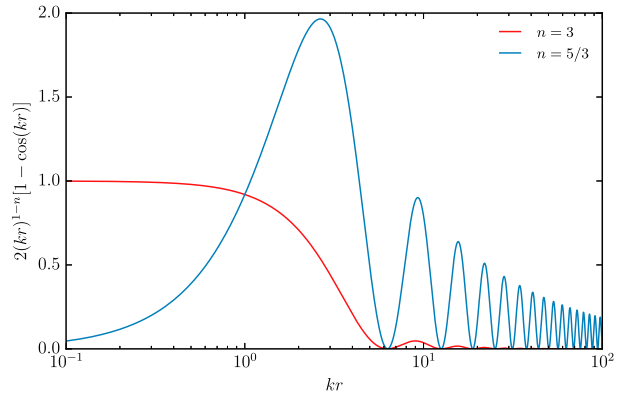


FIG. A1. Integrand of [\(A2\)](#) for spectral slopes $n = 5/3$ and $n = 3$. The integrand is multiplied by kr to compensate for the logarithmic shrinking.

separations do not reflect mesoscale dynamics. While wavenumber spectra show a rough equipartition between the rotational and divergent components of horizontal kinetic energy over a wide mesoscale range, structure functions exhibit a clear dominance of rotational energy. This is due to the nonlocal nature of structure functions, which leads to an imprint of the large rotational component at synoptic scales on the structure functions at mesoscale separations.

We here use the 2002–10 MOZAIC data with selection criteria similar to those used in [Callies et al. \(2014\)](#), making no distinction between data above and below the tropopause. Only data from northern midlatitudes (30° – 60° latitude) and above 350 hPa are used. Rare velocity spikes are removed by dismissing data that change by more than 10 m s^{-1} from one data point to the next. Within the remaining data, we use all flight segments that are at least 6000 km in length and have enough data coverage such that the average spacing is at most 1.2 km. A maximum of a 2° horizontal deviation from a best-fit great circle and a maximum of 1000 m from the mean altitude are allowed. This results in a total of 751 segments.^{A2}

The locations and velocities are transformed into a coordinate system aligned with the flight track determined by the best-fit great circle. As opposed to the interpolation onto a regular grid used in [Callies et al. \(2014\)](#), we now treat the data points as being equally spaced with the average spacing, because the locations have large rounding errors (longitude and latitude

^{A1} Note that this is the relation to the 1D spectrum. If the flow is statistically isotropic, the structure function can also be related to the 2D isotropic spectrum $S^a(k_n)$ by $\Delta^a(r) = 2 \int_0^\infty S^a(k_n) [1 - J_0(k_n r)] dk_n$, where J_0 is the zeroth-order Bessel function of the first kind. The properties of this transformation are very similar to the ones for 1D spectra discussed in the following.

^{A2} These are more than in [Callies et al. \(2014\)](#), because we now fit the great circle after removing the low-altitude data from takeoff and landing, which results in more segments satisfying the 2° -horizontal-deviation criterion. None of the results are affected by this change in data selection.

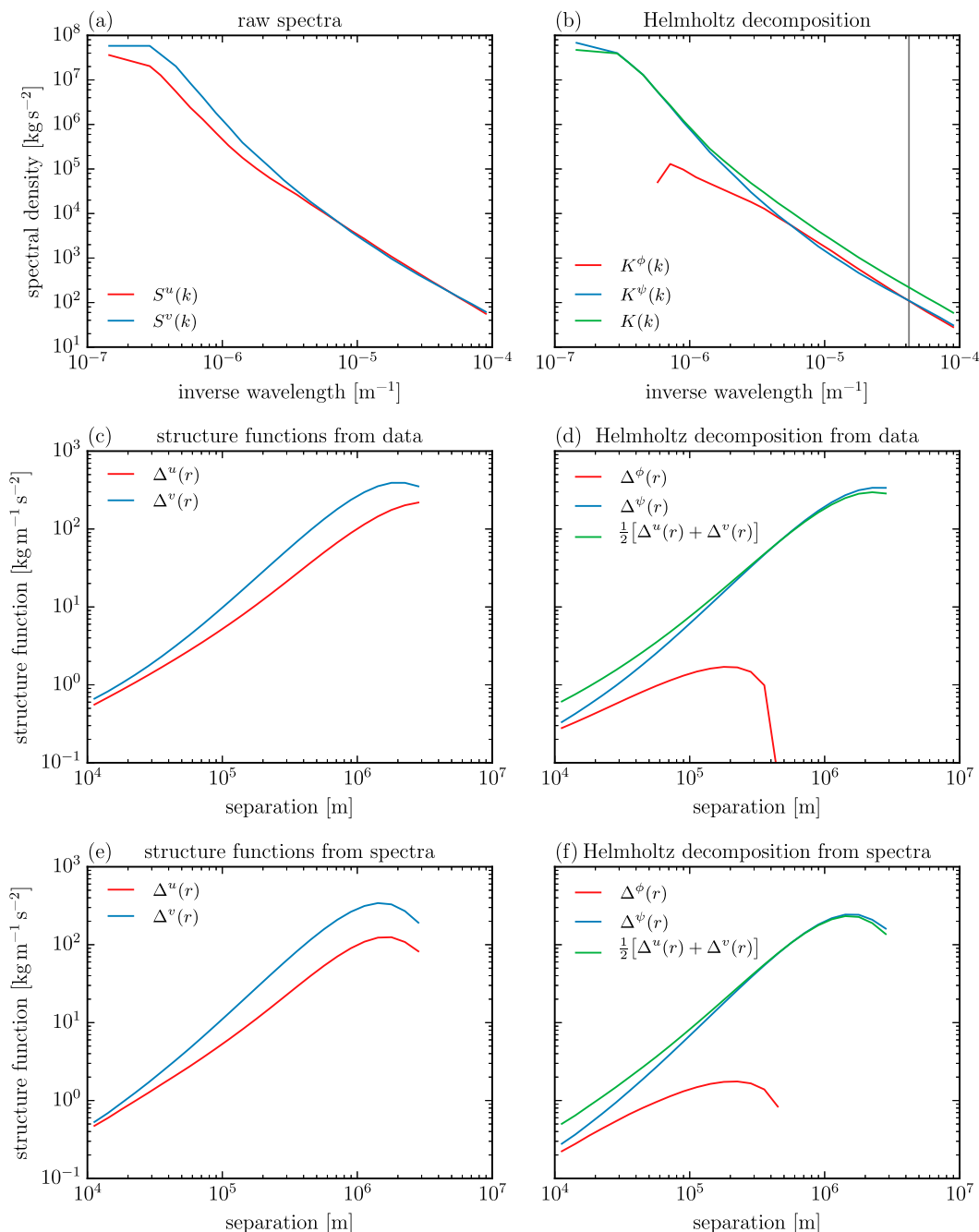


FIG. A2. Spectra, structure functions, and their respective Helmholtz decompositions from the full MOZAIC data. Shown are (a) the spectra and (b) their Helmholtz decomposition, equivalent to Callies et al. (2014); (c) the structure functions computed directly from the data and (d) their decomposition; and (e) the structure functions and (f) their decomposition computed from their respective spectral representation in (a) and (b) using (A2). The minimum separation $r_0 = 10$ km roughly corresponds to the wavenumber marked in (b).

reported to 0.01°). This change in data processing only affects the scales near the Nyquist wavenumber and has no effect on the results presented, which are restricted to wavenumbers smaller than $k = 2\pi/10$ km. The spectral estimates are obtained by applying a Hann window to all

segments, Fourier transforming, and averaging over segments and wavenumbers in 30 wavenumber bins uniformly partitioning the logarithmic wavenumber space between $k = 2\pi/10000$ km and $k = 2\pi/10$ km. Wavenumber bins with less than 150 Fourier components are discarded.

The along- and across-track velocity spectra $S^u(k)$ and $S^v(k)$ and the Helmholtz decomposition of the horizontal kinetic energy $K(k)$ into rotational and divergent components $K^\psi(k)$ and $K^\phi(k)$ show the same result as in Callies et al. (2014) (Figs. A2a,b). The synoptic range is strongly dominated by the rotational component, and the mesoscale range exhibits rough equipartition between the rotational and the divergent components, with a slight dominance of the divergent component around a wavelength of 100 km.

We compute from the same data the structure functions of along-track and across-track velocity $\Delta^u(r)$ and $\Delta^v(r)$. Applying the Helmholtz decomposition (Lindborg 2015)

$$2\Delta^\psi(r) = \Delta^v(r) + \int_0^r [\Delta^v(s) - \Delta^u(s)] \frac{ds}{s}, \quad \text{and} \quad (\text{A3})$$

$$2\Delta^\phi(r) = \Delta^u(r) - \int_0^r [\Delta^v(s) - \Delta^u(s)] \frac{ds}{s} \quad (\text{A4})$$

to these structure functions produces a partitioning similar to Lindborg's stratospheric case (Figs. A2c,d). There is a strong dominance of the rotational component at synoptic-scale separations and a modest dominance of the rotational component at mesoscale separations. It is confirmed that these structure functions are equivalent with the spectra by transforming the spectra into structure functions using (A2) (Figs. A2e,f).

This shows that, even though there is a rough equipartition between rotational and divergent kinetic energy over a wide range of mesoscales, as shown by the spectra in Figs. A2a,b, structure functions do not diagnose this equipartition. Instead, they show a significantly larger rotational component at mesoscale separations. This dominance of the rotational component, however, is reflective of a dominance at smaller wavenumbers and does not reflect variability at the mesoscales themselves.

Lindborg (2015) shows the structure functions down to separations as small as 2 km. We omit any separations below 10 km to be able to accurately estimate the structure functions from the spectra. Note that the first zero of the integrand in (A2) is at $kr = 2\pi$, so a spectral cutoff at wavelength $\lambda_0 = 2\pi/k_0 = 10$ km allows a somewhat accurate estimate of the structure function down to a separation $r_0 = 2\pi/k_0 = 10$ km. To aid the comparison between the structure functions and spectra, we marked in Fig. A2b the wavenumber corresponding to the maximum contribution to the structure function at minimum separation $r_0 = 10$ km if the spectrum were a $k^{-5/3}$ power law.

This comparison of equivalent spectra and structure functions emphasizes the point that spectra are more informative about the dynamics, because the spectral

estimate at a certain scale represents variability at that scale if care has been taken in windowing the finite data series. The value of a structure function at separation r , on the other hand, can reflect variability at a much larger scale. In the case of aircraft data, the strong rotational component at synoptic scales affects the structure function at mesoscale separations.

REFERENCES

- Babiano, A., C. Basdevant, and R. Sadourny, 1985: Structure functions and dispersion laws in two-dimensional turbulence. *J. Atmos. Sci.*, **42**, 941–949, doi:10.1175/1520-0469(1985)042<0941:SFADLI>2.0.CO;2.
- Baumeister, J. T., S. D. Eckermann, P. A. Newman, L. Lait, K. R. Chan, M. Loewenstein, M. H. Proffitt, and B. L. Gary, 1996: Stratospheric horizontal wavenumber spectra of winds, potential temperature, and atmospheric tracers observed by high-altitude aircraft. *J. Geophys. Res.*, **101**, 9441–9470, doi:10.1029/95JD03835.
- Bartello, P., 1995: Geostrophic adjustment and inverse cascades in rotating stratified turbulence. *J. Atmos. Sci.*, **52**, 4410–4428, doi:10.1175/1520-0469(1995)052<4410:GAAICI>2.0.CO;2.
- Batchelor, G. K., 1953: *The Theory of Homogeneous Turbulence*. Cambridge University Press, 197 pp.
- Bierdel, L., C. Snyder, S.-H. Park, and W. C. Skamarock, 2016: Accuracy of rotational and divergent kinetic energy spectra diagnosed from flight-track winds. *J. Atmos. Sci.*, **73**, 3273–3286, doi:10.1175/JAS-D-16-0040.1.
- Bühler, O., J. Callies, and R. Ferrari, 2014: Wave–vortex decomposition of one-dimensional ship-track data. *J. Fluid Mech.*, **756**, 1007–1026, doi:10.1017/jfm.2014.488.
- Callies, J., R. Ferrari, and O. Bühler, 2014: Transition from geostrophic turbulence to inertia–gravity waves in the atmospheric energy spectrum. *Proc. Natl. Acad. Sci. USA*, **111**, 17 033–17 038, doi:10.1073/pnas.1410772111.
- Charney, J. G., 1971: Geostrophic turbulence. *J. Atmos. Sci.*, **28**, 1087–1095, doi:10.1175/1520-0469(1971)028<1087:GT>2.0.CO;2.
- Dee, D. P., and Coauthors, 2011: The ERA-Interim reanalysis: Configuration and performance of the data assimilation system. *Quart. J. Roy. Meteor. Soc.*, **137**, 553–597, doi:10.1002/qj.828.
- Dewan, E. M., 1979: Stratospheric wave spectra resembling turbulence. *Science*, **204**, 832–835, doi:10.1126/science.204.4395.832.
- Gage, K. S., 1979: Evidence for a $k^{-5/3}$ law inertial range in mesoscale two-dimensional turbulence. *J. Atmos. Sci.*, **36**, 1950–1954, doi:10.1175/1520-0469(1979)036<1950:EFALIR>2.0.CO;2.
- Hamilton, K., Y. O. Takahashi, and W. Ohfuchi, 2008: Mesoscale spectrum of atmospheric motions investigated in a very fine resolution global general circulation model. *J. Geophys. Res.*, **113**, D18110, doi:10.1029/2008JD009785.
- Lilly, D. K., 1983: Stratified turbulence and the mesoscale variability of the atmosphere. *J. Atmos. Sci.*, **40**, 749–761, doi:10.1175/1520-0469(1983)040<0749:STATMV>2.0.CO;2.
- Lindborg, E., 2006: The energy cascade in a strongly stratified fluid. *J. Fluid Mech.*, **550**, 207–242, doi:10.1017/S0022112005008128.
- , 2015: A Helmholtz decomposition of structure functions and spectra calculated from aircraft data. *J. Fluid Mech.*, **762**, R4, doi:10.1017/jfm.2014.685.
- McComas, C. H., and P. Müller, 1981: The dynamic balance of internal waves. *J. Phys. Oceanogr.*, **11**, 970–986, doi:10.1175/1520-0485(1981)011<0970:TDBOIW>2.0.CO;2.

- Nastrom, G. D., and K. S. Gage, 1985: A climatology of atmospheric wavenumber spectra of wind and temperature observed by commercial aircraft. *J. Atmos. Sci.*, **42**, 950–960, doi:[10.1175/1520-0469\(1985\)042<0950:ACOAWS>2.0.CO;2](https://doi.org/10.1175/1520-0469(1985)042<0950:ACOAWS>2.0.CO;2).
- , D. C. Fritts, and K. S. Gage, 1987: An investigation of terrain effects on the mesoscale spectrum of atmospheric motions. *J. Atmos. Sci.*, **44**, 3087–3096, doi:[10.1175/1520-0469\(1987\)044<3087:AIOTEO>2.0.CO;2](https://doi.org/10.1175/1520-0469(1987)044<3087:AIOTEO>2.0.CO;2).
- Pan, L. L., and Coauthors, 2010: The Stratosphere–Troposphere Analyses of Regional Transport 2008 experiment. *Bull. Amer. Meteor. Soc.*, **91**, 327–342, doi:[10.1175/2009BAMS2865.1](https://doi.org/10.1175/2009BAMS2865.1).
- Polzin, K. L., and Y. V. Lvov, 2011: Toward regional characterizations of the oceanic internal wavefield. *Rev. Geophys.*, **49**, RG4003, doi:[10.1029/2010RG000329](https://doi.org/10.1029/2010RG000329).
- Skamarock, W. C., S.-H. Park, J. B. Klemp, and C. Snyder, 2014: Atmospheric kinetic energy spectra from global high-resolution nonhydrostatic simulations. *J. Atmos. Sci.*, **71**, 4369–4381, doi:[10.1175/JAS-D-14-0114.1](https://doi.org/10.1175/JAS-D-14-0114.1).
- Tulloch, R., and K. S. Smith, 2006: A theory for the atmospheric energy spectrum: Depth-limited temperature anomalies at the tropopause. *Proc. Natl. Acad. Sci. USA*, **103**, 14 690–14 694, doi:[10.1073/pnas.0605494103](https://doi.org/10.1073/pnas.0605494103).
- Vallis, G. K., G. J. Shutts, and M. E. B. Gray, 1997: Balanced mesoscale motion and stratified turbulence forced by convection. *Quart. J. Roy. Meteor. Soc.*, **123**, 1621–1652, doi:[10.1002/qj.49712354209](https://doi.org/10.1002/qj.49712354209).
- VanZandt, T. E., 1982: A universal spectrum of buoyancy waves in the atmosphere. *Geophys. Res. Lett.*, **9**, 575–578, doi:[10.1029/GL009i005p00575](https://doi.org/10.1029/GL009i005p00575).
- Zhang, F., J. Wei, M. Zhang, K. P. Bowman, L. L. Pan, E. Atlas, and S. C. Wofsy, 2015: Aircraft measurements of gravity waves in the upper troposphere and lower stratosphere during the START08 field experiment. *Atmos. Chem. Phys.*, **15**, 7667–7684, doi:[10.5194/acp-15-7667-2015](https://doi.org/10.5194/acp-15-7667-2015).